Title

A High-Speed, Heavy-Load and Direction Controllable Photothermal Pneumatic Floating Robot

Authors

Xuande Lv, Wenzhong Wang, Adam J. Clancy and Haifeng Yu*

Affiliations

Mr. X. Lv, Dr. W. Wang, Prof. Dr. H. Yu

Department of Material Science and Engineering

College of Engineering

Key Laboratory of Polymer Chemistry and Physics of Ministry of Education, Peking University, Beijing 100871, China

E-mail: yuhaifeng@pku.edu.cn

Dr. A. J. Clancy

Department of Chemistry, UCL, 20 Gordon St., London WC1H 0AJ, UK

Abstract

Light controlling actuators are promising in many fields due to their contactless and eco-efficiency features. However, their application in liquid environments is complicated by the challenges of rapid deformation in liquids, light absorption by the liquid media, and environmental contamination. Here, we design a photothermal pneumatic floating robot (PPFR) applicable to shallow liquid. Light energy is converted into thermal energy of air by an isolated photothermal composite, which is converted into mechanical energy of liquid to drive the robot. By understanding and controlling the photothermal actuation, the PPFR can achieve an average velocity of 13.1 mm s^{-1} in water, and can be modified for remote on-demand differential steering, and self-sustained oscillation. The PPRF may be modified to provide a lifting mechanism, capable of moving four times the PPFR mass.. Various shapes and materials are suitable for the PPFR providing a platform for liquid surface transporting, water sampling, pollutant collecting, underwater photography and photocontrol robots in shallow water.

Summary

A light-driven robot, prepared without chemical synthesis, targeted at fast and heavy-load vehicle in shallow water.

INTRODUCTION

Stimulus-responsive swimming actuators hold potential across a range of applications in liquid environments [1-6]; with various driving mechanisms explored, utilizing vibration [4, 7], interfacial tension [2, 8], deformation [1, 3, 6, 9, 10], and mass center displacement [5, 11]. The energy for driving actuators can be thermal [2, 5, 12], photonic [1, 3, 4, 6, 7, 9-11], magnetic [8, 13], or chemical [14]. Light is arguably the ideal option, being a non-contact light source, allowing actuating devices to be small and lightweight without carrying a power supply. The light power itself is clean, adjustable/programmable and may make use of highly ambient (e.g. solar) light, or directional light (e.g. laser) to enable accurate and remote control of movement. However, light-responsive swimming actuators often face the challenges of contact pollution, small deformation, and poor diaphaneity, which may be mitigated through using light to power photothermal actuation.

Thermal energy has always been an important energy source in scientific research and industrial development. However, difficulty in controlling conduction, dissipation and thermal gradients prevents efficient, and spatially accurate, application for long-distance power transfer. The photothermal effect provides elegant way to solve the above limitation. Energy transport between power source and actuator may occur photonically through light-transparent media with high spatio-temporal resolution and negligible loss. When light irradiates photothermal reagents, the surrounding media heat [15, 16], which may be used to drive a local actuator through thermally-induced interfacial tension changes [2], deformation [17, 18], or mass center displacement [5, 19]. Generally, gases have larger thermal expansion coefficient and smaller volumetric heat capacity than most solids components and liquids components albeit at lower thermal conductivity. Here, we create a light-operated swimming actuator with high speed, heavy payload capacity, on-demand direction control, and good transparency. To obtain a light-induced deformation large enough in a short time, we develop a photothermal pneumatic device by using the deformation of air, for a range of underwater mechanical motions to create a family of photothermal pneumatic floating robots (PPFRs).

When the PPFR is swimming, most of the photothermal energy is converted and used to overcome the liquid resistance, and the horizontal component of the liquid resistance acts as the driving force. Relatedly, some light-controlling underwater robots use photoinduced deformation of polymer materials, and the deformation causes the water reaction force to drive robots swim [1, 3, 6]. The main challenge of light-controlling underwater robots is to achieve deformation large enough underwater in a short time, because water suppresses the photoinduced deformation as well as absorbs part of the light.

RESULTS AND DISCUSSION

Structure Design of the PPFR

The design of the PPFR was based around a duck (Fig. 1B), with a floating body on the water surface, propulsed by drag from a swinging quasi-rhombus 'foot', designed to maximize water resistance, as has been seen in previous swimming robots [34]. The paddle is connected to a hollow transparent tube which leads up to the floating body consisting of a hollow transparent sphere housing the photothermal material (Fig. 1A). The device rests on the water with the tube/foot submerged, sealing the air within the body and tube; the pneumatics in the device arise from thermal control of this air, acting as a piston. Once heated or cooled, the enclosed air in this piston expands/contracts respectively in accordance with the ideal gas law. Upon expansion of air, water in the tube is displaced, while contraction of the air leads to partial (re)filling of the tube with water [17, 20, 23]. The use of pneumatics as a driving force for the device makes it well suited in the future for elastic soft robots [20-22]. By irradiating the photothermal composite through the transparent body, part of the transmitted light energy is converted into the thermal energy of air, which is subsequently converted into mechanical energy for driving the robot.

Many photothermal agents are known including carbon nanomaterials [17, 24], azo compounds [17], polypyrrole [25-27], polydopamine [2, 28], semiconducting metal chalcogenides [29, 30], and metal nanoparticles [31-33]. Among these, graphene-based materials are widely used, with light absorbance over 270 – 2500 nm (Fig. S1A), suitable for synthetic and solar light sources. Here, a reduced graphene oxide-doped sponge was selected, with the porous substrate maximizing surface area for heat-transfer to mitigate the slow intrinsic kinetics of heat transfer of a gas (Fig. S1, B to E). In contrast to submerged-photothermal devices, the use of a floating air chamber ensures that, the light illuminates the photothermal composite without passing through any liquid, and the photothermal agents does not contact or pollute any liquid.

Swimming Mechanism of PPFR

There are two behaviors involved with the motion of the PPFR associated with light irradiation and relaxation once illumination ceases. For the former, when light irradiates the photothermal composite, the air heats and expands, expelling liquid as the pressure in the air chamber is higher than the liquid pressure at the tail end of the tube, until the pressures match. The length of air column in tube increases, the center of buoyancy lowers, and the end of tube rises under buoyancy, with the rising paddle pushing liquid backward to accelerate the robot forward (Fig. 1C). When light irradiation is stopped, a relaxation process occurs with air cooling and contracting, lowering the pressure in the air chamber below the liquid pressure at the tail end of the tube. The buoyancy decreases as the tube refills with water, leading to the paddle falling, pushing liquid forward and accelerating the robot backward. (Fig. 1D). While the PPFR is dragged by the liquid resistance in both periods (in opposite directions), it only receives energy input during irradiation, while the relaxation process is passive. Thus, the horizontal movements of two periods are asymmetric, and the forward horizontal displacement from irradiation is larger than the backward horizontal displacement during relaxation. Hence, the net result of irradiation and relaxation is the PPFR moving forward (Fig. 2, A and B). Though a PPFR moves backward in relaxation, the resultant conditions (low air pressure, high center of buoyancy) are prerequisites for the forward motion under irradiation, with cycling the two processes leading to sustained net-forward motion. Therefore, a PPFR can run continuously under intermittent lighting, with the PPFR developed here reaching averaged velocities up to 13.1 mm s^{-1}.

(Fig. 2A). The concept of intermittent short-time irradiation control for devices has been utilized previously [1, 3, 17, 39] and is seen commonly in nature, notably in photosynthesis [38], although it should be noted that the input type and approach to control varies significantly from continuous irradiation actuators [2, 11, 36, 37] and other continuous irradiation approaches (e.g. photothermal therapy [24, 31], photothermal desalination [35]).

Light Driving behaviors of PPFR

The intermittent nature of the powering the PPFR provides intrinsic programmability to the motion, through control over the duration of irradiation/non-exposure times, with different irradiation programs providing different PPFR performances. We plot the displacement-time curve and measure the averaged horizontal velocity (v) of the movement cycles. (Fig. 2A) To calculate v, we divide the total displacement by the total movement time. The energy efficiency EE can be calculated by the following formula,

$$EE = \frac{\frac{1}{2}mv^2}{PSt}$$

where m is the mass of PPFR, P is the power density of the irradiation, S is the irradiation area on the photothermal composite, and t is the irradiation time in one cycle. For a specified PPFR under controlled irradiation, the velocity and EE can be mapped as a function of both irradiation and (non-irradiated) relaxation time. As strong horizontal forces propelling the PPFR can be related to large air temperature gradients causing rapid changes in volume, the temperature profile of the photothermal element provides insight into the timescale of ideal irradiation/non-irradiation parameters. The temperature-time curve of graphene is known to follow exponential trends, both during photothermal heating and ambient cooling [17]. Here, more than 94.0% of air temperature gradient happens in the initial 8s in both temperature-rise and temperature-fall stages (Fig. 3), so irradiation/relaxation times were limited to ≤ 8 s.

Here, intermittent 980 nm light irradiation (power density of 170 mW cm^{-2} power density, 2.35 cm^2) was tested with 3 – 9 s irradiation and 5 – 8 s relaxation highlighting the controllable behavior, achieving average speeds of 6.4 – 13.1 mm s^{-1} (Movie S1) and energy efficiencies of $9 \times 10^{-8} - 3.0 \times 10^{-7}$ (Table 1, Fig X). The highest performance occurring at 6 s irradiation (5 s non-irradiated), highlighting the success of using temperature profiles to design parameter space; more rapidly hating photothermal elements may facilitate faster speeds for future devices.

In addition to directed synthetic irradiation, solar power is feasible, using intermittent shading to stop irradiation and enter the relaxation phase. While sunlight had a lower power density (37 mW cm^{-2}), it was offset by the higher irradiated area (9.0 cm^2), facilitating average speeds of 7.3 – 9.6 mm s^{-1}（Fig. 4, Movie S2）providing the fastest sunlight-driven robot swimming speed reported to date.

Leverage of PPFR

Because the air chamber is partially submerged, a load may be hung from the bottom of the chamber and the PPRF; the behavior of the device depends on the density of the payload, (Fig. 5). When the density of the load is about equal to the density of the surrounding water, the system was capable of towing 31.7 g (~4 × the PPFR, 8.3g) at an average speed of 3.9 mm s^{-1}. This response is the highest payload for any light-driven swimming robot at this speed to the authors knowledge.

However, when the payload density is notably higher than water (≥1.1 g cm^{-3}), under irradiation, the PPFR tilted up and down, without significant directional motion across the water surface. Instead, the system may be seen as a lever rotating about a hypothetical fulcrum near water surface. Under irradiation, the changing buoyant force counterbalancing gravity rotates the lever (as seen for the swimming motion), but the additional load impedes the rotation, leading to near-symmetric forwards/backwards accelerations and no net movement across an irradiation/relaxation cycle. The rotational drag comes from the resultant of buoyant force and gravity to the hanging load. (Fig. 5A) By adjusting the load density to about 1.0 g cm^{-3}, the rotation drag can negated. (Fig. 5B) Though the velocity of PPFR is decreased, the rotation of the loaded PPFR is unlimited as there is no extra load, which provides a large enough water resistance to drive the loaded PPFR. (Fig. 5C, Movie S3) Hence, by adjusting the load density, the total weight may be enlarged, with potential for different PPFR tasks, such as water sampling, pollutant collecting and underwater photography.

Integration and on-demand control of PPFRs

With the driving mechanism in place, the PPFR may be modified to provide more advanced behaviors, such as controllable directionality and continuous mobility under non-intermittent light sources.

Real-world swimming robots require controllable mobility beyond simply moving forward. Taking advantage of the programable nature of the iiradiation/relaxation cycling, multiple PPFR drivers may be connected to a fixed device to achieve on-demand turning (Fig. 6A). As a demonstrator, two identical PPFRs were connected at their air chambers. To go straight, both PPFR may be irradiated with the same power density. Conversely, turning is possible by irradiating a single PPFR to provide differential steering; for example to turn left, only the right PPFR is irradiated, causing the right hand side of the device to accelerate forward, (Fig. 6B) while only irradiating the left device causes a right turn (Movie S4).

Self-sustained oscillating PPFR

The use of a non-modulating light sources is preferable in many situations and is an advantage intrinsic to continuous irradiation actuators. For internment irradiation devices, self-sustained oscillation can be used to provide cycling under a constant external light source [10, 40, 41], which may be provided through self-shadowing. Here, the side of the air chamber is covered with opaque tape (Fig. 7A, Movie S5). Upon irradiation of the uncovered photothermal composite from above, the PPFR tube rose and the air chamber rotated on the liquid surface. In the rotated position, the photothermal composite was shaded by the tape, initiating the relaxation stage (Fig. 7B), causing the tube to fall and rotating the chamber to expose the photothermal composite to irradiation again. In this manner, the PPFR achieves self-sustained oscillating irradiation and sustainable movement under quasi-uniform light, such as sunlight.

CONCLUSION

In summary, an environmentally friendly light-operated photothermal pneumatic floating robot (PPFR) has been developed with high speed, directional control, and high loadbearing capacity. Light energy is effectively converted into the kinetic energy of the PPFR through a photothermal composite, and by understanding and optimizing the photothermally-driven mechanics, an average speed of 13.1 mm s^{-1} has been achieved in shallow water. The PPFR may be modified to operate under continuous irradiation, or to enable remote differential steering. The modular design does not rely on one specific photothermal agent, so may be fitted with any commercial photothermal agent for driving with a matching light source. Through use of a leverage model the payload capacity of the PPFR to at least four times of its own mass. This PPFR is a potential platform for liquid surface transporting, water sampling, pollutant collecting, underwater photography and photocontrol robots in shallow water.

MATERIALS AND METHODS

Materials

Reduced graphene oxide (XFSG04, Nanjing Xianfeng Nanomaterial Technology Co., Ltd.), hollow polymethylmethacrylate halfsphere and polyethylene terephthalate capsule (Yiwu Guangren Trading Co., Ltd.), polyurethane sponge (Freudenberg), polyvinyl chloride sheet (0.2 mm in thickness, Shandong JTC Plastic Products Co., Ltd.), polypropylene tube (4 mm in diameter, Shenzhen Chenjing Plastic Products Co., Ltd), silicone tube (Ningbo Yili New Materials Co., Ltd.), epoxy adhesive (WD3620, Shanghai Kangda New Materials Co., Ltd.), ethanol and glass capillary (Beijing

Tongguang chemical company).

Fabrication of the Photothermal Composites

Reduced graphene oxide (XXX g) was mixed with ethanol (XXX mL) and sonicated in a bath sonicator/with a probe sonicator for XXX min. The resultant dispersion was injected into a piece of 3 × 3 × 0.2 cm polyurathane sponge and dried at 50 °C for XXX hours to give the photothermal composite, containing 33 wt.% reduced graphene oxide (as measured by XXX).

Fabrication of the PPFR

The photothermal composite was placed into a hollow polymethylmethacrylate sphere with a diameter of 4 cm. A hole was drilled into the sphere and a polypropylene tube (4 mm inner/outer diameter, XXX mm length) was inserted. The gap between sphere and tube was sealed with an epoxy adhesive. A rhomboid polyvinyl chloride sheet (XXX × XXX mm) was adhered to the end of the tube wall as a paddle. A metal clip was affixed on the paddle-end of the tube; the final PPFR weighed 8.3 g. Analogous designs of different sizes and with different materials were shown to also be feasible.

The driving of a PPFR

A light source (HTLD-4II, Shenzhen HEIGHT-LED Co., Ltd.) was set to irradiate the photothermal composites in the transparent air chamber. The first way, the PPFR went forward or backward when the light source was on or off. The second way, the PPFR went forward or backward when light point to photothermal composite or not, with the light source on all the time.

Characterizations

The surface temperature of the air chamber (containing a sponge doped with graphene inside) was monitored using an infrared thermometer (CEM DT-810) equipped with a digital camera. The movement movies were converted to displacement-time data with the software Adobe After Effects CC 2018. The microscopic structure of the doped sponge was observed with a scanning electron microscope (SEM; S-4800, Hitachi). light absorption of the reduced graphene oxide-doped sponge was performed through UV-Vis-NIR spectroscopy (190 – 3300 nm, Lambda 750, Perkin Elmer).

References

1. Shahsavan, H., et al., *Bioinspired underwater locomotion of light-driven liquid crystal gels.* Proceedings of the National Academy of Sciences of the United States of America, 2020. **117**(10): p. 5125-5133.
2. Yang, R.-L., et al., *Superhydrophobic Photothermal Paper Based on Ultralong Hydroxyapatite Nanowires for Controllable Light-Driven Self-Propelled Motion.* ACS Sustainable Chemistry & Engineering, 2019. **7**(15): p. 13226-13235.
3. Zhao, Y., et al., *Soft phototactic swimmer based on self-sustained hydrogel oscillator.* Science Robotics, 2019. **4**(33).
4. Ma, S., et al., *A Light-Activated Polymer Composite Enables On-Demand Photocontrolled Motion: Transportation at the Liquid/Air Interface.* Angewandte Chemie International Edition, 2019. **58**(9): p. 2655-2659.
5. Wang, L., et al., *A Bioinspired Swimming and Walking Hydrogel Driven by Light-Controlled Local Density.* Advanced Science, 2015. **2**(6).
6. Huang, C., et al., *Miniaturized Swimming Soft Robot with Complex Movement Actuated and Controlled by Remote Light Signals.* Scientific Reports, 2015. **5**(1).
7. da Cunha, M.P., et al., *Unravelling the photothermal and photomechanical contributions to actuation of azobenzene-doped liquid crystal polymers in air and water.* Journal of Materials Chemistry C, 2019. **7**(43): p. 13502-13509.
8. Grosjean, G., et al., *Surface swimmers, harnessing the interface to self-propel.* European Physical Journal E, 2018. **41**(11).
9. Li, C., et al., *Light-Driven Expansion of Spiropyran Hydrogels.* Journal of the American Chemical Society, 2020. **142**(18): p. 8447-8453.
10. Yang, L., et al., *An Autonomous Soft Actuator with Light-Driven Self-Sustained Wavelike Oscillation for Phototactic Self-Locomotion and Power Generation.* Advanced Functional

Materials, 2020. **30**(15).
11. Singh, D.P., et al., *Photogravitactic Microswimmers.* Advanced Functional Materials, 2018. **28**(25).
12. Godaba, H., et al., *A Soft Jellyfish Robot Driven by a Dielectric Elastomer Actuator.* Ieee Robotics and Automation Letters, 2016. **1**(2): p. 624-631.
13. Xu, T., et al., *Millimeter-scale flexible robots with programmable three-dimensional magnetization and motions.* Science Robotics, 2019. **4**(29).
14. Jin, C., et al., *Chemotactic droplet swimmers in complex geometries.* Journal of Physics-Condensed Matter, 2018. **30**(5).
15. Bisoyi, H.K., A.M. Urbas, and Q. Li, *Soft Materials Driven by Photothermal Effect and Their Applications.* Advanced Optical Materials, 2018. **6**(15).
16. Yang, M., et al., *Photoresponsive Actuators Built from Carbon-Based Soft Materials.* Advanced Optical Materials, 2019. **7**(16).
17. Lv, X., W. Wang, and H. Yu, *A Bioinspired Photothermal Pneumatic Device Enabling Optical Manipulation of Microfluid toward Precise Control of Microreactions.* Advanced Engineering Materials, 2019.
18. Hua, D., et al., *3D printing of shape changing composites for constructing flexible paper-based photothermal bilayer actuators.* Journal of Materials Chemistry C, 2018. **6**(8): p. 2123-2131.
19. Yu, L. and H.F. Yu, *Light-Powered Tumbler Movement of Graphene Oxide/Polymer Nanocomposites.* Acs Applied Materials & Interfaces, 2015. **7**(6): p. 3834-3839.
20. Terryn, S., et al., *Self-healing soft pneumatic robots.* Science Robotics, 2017. **2**(9).
21. Shepherd, R.F., et al., *Multigait soft robot.* Proceedings of the National Academy of Sciences, 2011. **108**(51): p. 20400-20403.
22. Tang, Y., et al., *Leveraging elastic instabilities for amplified performance: Spine-inspired high-speed and high-force soft robots.* Science Advances, 2020. **6**(19).
23. Greer, J.D., et al., *Series Pneumatic Artificial Muscles (sPAMs) and Application to a Soft Continuum Robot.* IEEE International Conference on Robotics and Automation : ICRA : [proceedings]. IEEE International Conference on Robotics and Automation, 2017. **2017**: p. 5503-5510.
24. Yang, K., et al., *Graphene in Mice: Ultrahigh In Vivo Tumor Uptake and Efficient Photothermal Therapy.* Nano Letters, 2010. **10**(9): p. 3318-3323.
25. Yang, K., et al., *In Vitro and In Vivo Near-Infrared Photothermal Therapy of Cancer Using Polypyrrole Organic Nanoparticles.* Advanced Materials, 2012. **24**(41): p. 5586-5592.
26. Wang, X., et al., *Ultrathin Polypyrrole Nanosheets via Space-Confined Synthesis for Efficient Photothermal Therapy in the Second Near-Infrared Window.* Nano Letters, 2018. **18**(4): p. 2217-2225.
27. Wang, X., et al., *Multilayer Polypyrrole Nanosheets with Self-Organized Surface Structures for Flexible and Efficient Solar-Thermal Energy Conversion.* Advanced Materials, 2019. **31**(19).
28. Yu, S., et al., *Dendritic Fe3O4@Poly(dopamine)@PAMAM Nanocomposite as Controllable NO-Releasing Material: A Synergistic Photothermal and NO Antibacterial Study.* Advanced Functional Materials, 2018. **28**(20).
29. Wang, R., et al., *Surface-Functionalized Modified Copper Sulfide Nanoparticles Enhance*

Checkpoint Blockade Tumor Immunotherapy by Photothermal Therapy and Antigen Capturing. Acs Applied Materials & Interfaces, 2019. **11**(15): p. 13964-13972.
30. Li, Q., et al., *Phase-Change Material Packaged within Hollow Copper Sulfide Nanoparticles Carrying Doxorubicin and Chlorin e6 for Fluorescence-Guided Trimodal Therapy of Cancer.* Acs Applied Materials & Interfaces, 2019. **11**(1): p. 417-429.
31. Huang, X.H., et al., *Cancer cell imaging and photothermal therapy in the near-infrared region by using gold nanorods.* Journal of the American Chemical Society, 2006. **128**(6): p. 2115-2120.
32. Riedel, R., et al., *Synthesis of gold-silica core-shell nanoparticles by pulsed laser ablation in liquid and their physico-chemical properties towards photothermal cancer therapy.* Nanoscale, 2020. **12**(5): p. 3007-3018.
33. Gherman, A.M.M., et al., *Plasmonic photothermal heating of gold nanostars in a real-size container: multiscale modelling and experimental study.* Nanotechnology, 2020. **31**(12).
34. Kashem, S.B.A., et al., *Design and Implementation of a Quadruped Amphibious Robot Using Duck Feet.* Robotics, 2019. **8**(3).
35. Yang, Y., et al., *Graphene-Based Standalone Solar Energy Converter for Water Desalination and Purification.* Acs Nano, 2018. **12**(1): p. 829-835.
36. Ma, S., et al., *A Light-Activated Polymer Composite Enables On-Demand Photocontrolled Motion: Transportation at the Liquid/Air Interface.* Angewandte Chemie-International Edition, 2019. **58**(9): p. 2655-2659.
37. Wang, Z., et al., *A Light-Powered Ultralight Tensegrity Robot with High Deformability and Load Capacity.* Advanced Materials, 2019. **31**(7).
38. Farquhar, G.D., M.H. Oleary, and J.A. Berry, *ON THE RELATIONSHIP BETWEEN CARBON ISOTOPE DISCRIMINATION AND THE INTER-CELLULAR CARBON-DIOXIDE CONCENTRATION IN LEAVES.* Australian Journal of Plant Physiology, 1982. **9**(2): p. 121-137.
39. Li, X., et al., *Photo-activated bimorph composites of Kapton and liquid-crystalline polymer towards biomimetic circadian rhythms of Albizia julibrissin leaves.* Journal of Materials Chemistry C, 2019. **7**(3): p. 622-629.
40. Lan, R., et al., *Near-Infrared Photodriven Self-Sustained Oscillation of Liquid-Crystalline Network Film with Predesignated Polydopamine Coating.* Advanced Materials, 2020.
41. Hu, Y., et al., *A Graphene-Based Bimorph Structure for Design of High Performance Photoactuators.* Advanced Materials, 2015. **27**(47): p. 7867-7873.

Acknowledgments: We thank Chinese Academy of Sciences for the scanning electron microscope. **Funding:** This work is supported by the National Key R&D Program of China (2018YFB0703702) and the National Natural Science Foundation of China (Grant No.s 51773002, 51921002). A J. C. would like to thank the Society for Chemical Industry and the Ramsay Memorial Fund for their support. **Author contribution:** X. L. designed and prepared the PPFR; performed the experiments; analysed the data; built the leverage model of PPFR and wrote the paper. W. W. and A. J. C. suggests the differential steering and edited the associated section. H. Y. directed the research and revised the paper. **Conflicts of interest**: There are no conflicts to declare. **Data and materials availability:** All data needed to evaluate the conclusions of the paper are available in the paper or the Supplementary Materials.

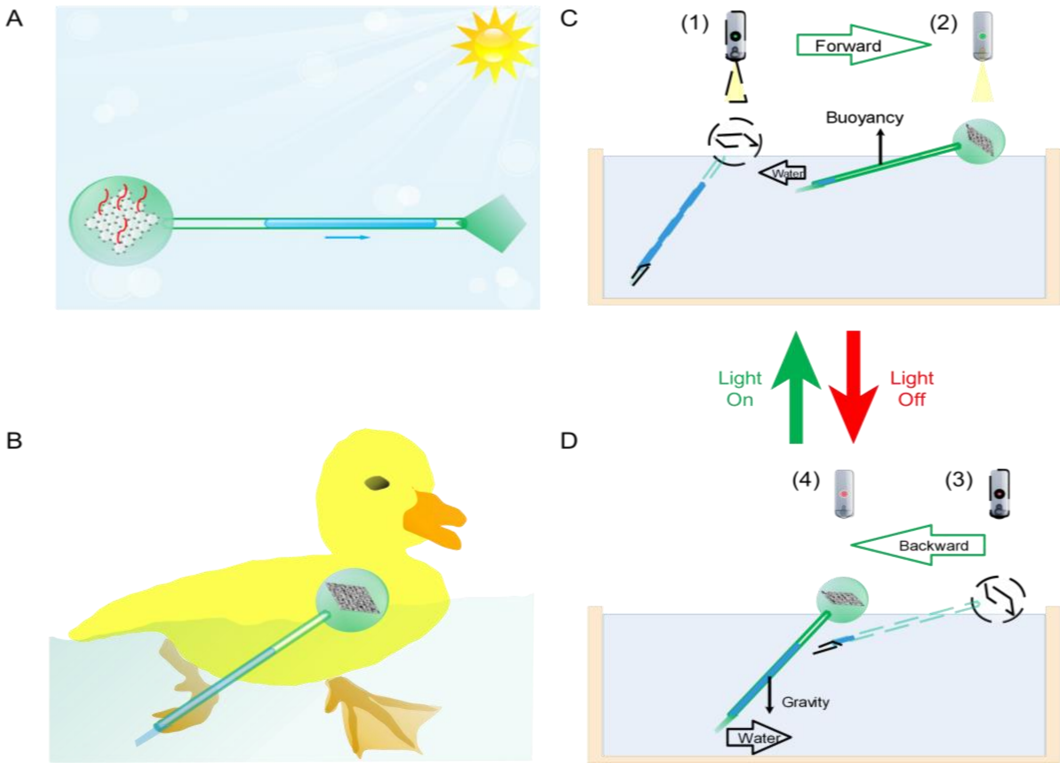

Fig. 1. Structure and swimming mechanism of PPFR. (**A**) Schematic illustration of a photothermal pneumatic floating robot (PPFR) exposed to light. (**B**) A painting illustrating the duck-foot inspired concept of the PPFR. (**C** and **D**) Schematic illustration of the forward and backward movement of PPFR. (Side view)

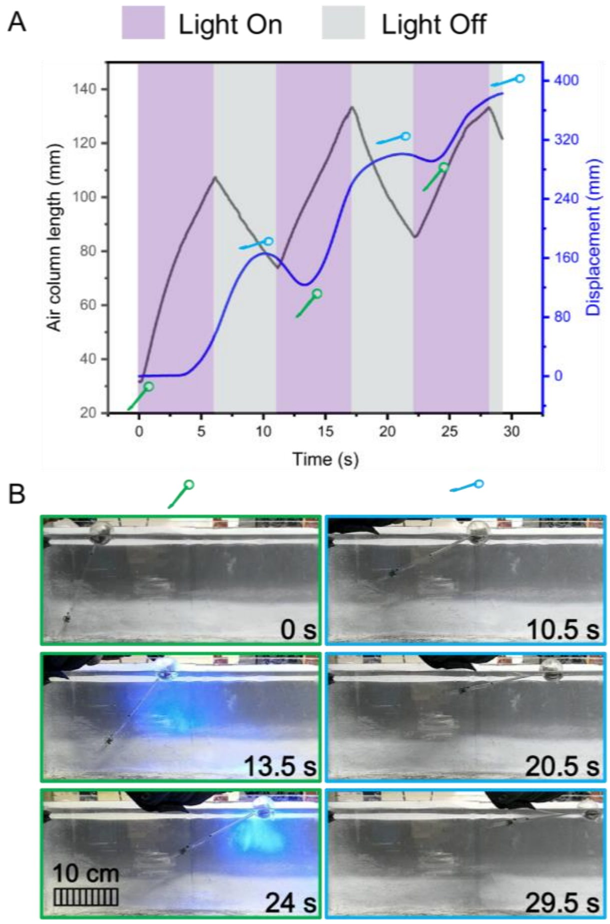

Fig. 2. Light driving performance of PPFR. (**A**) Air column length changing with time in a driving PPFR (black curve), horizontal displacement of the PPFR changing with time (blue curve), and diagrams of PPFR at the beginning of forward driving (in green) and at the beginning of backward driving (in blue). (**B**) Digital images showing the forward driving and backward driving of PPFR through time.

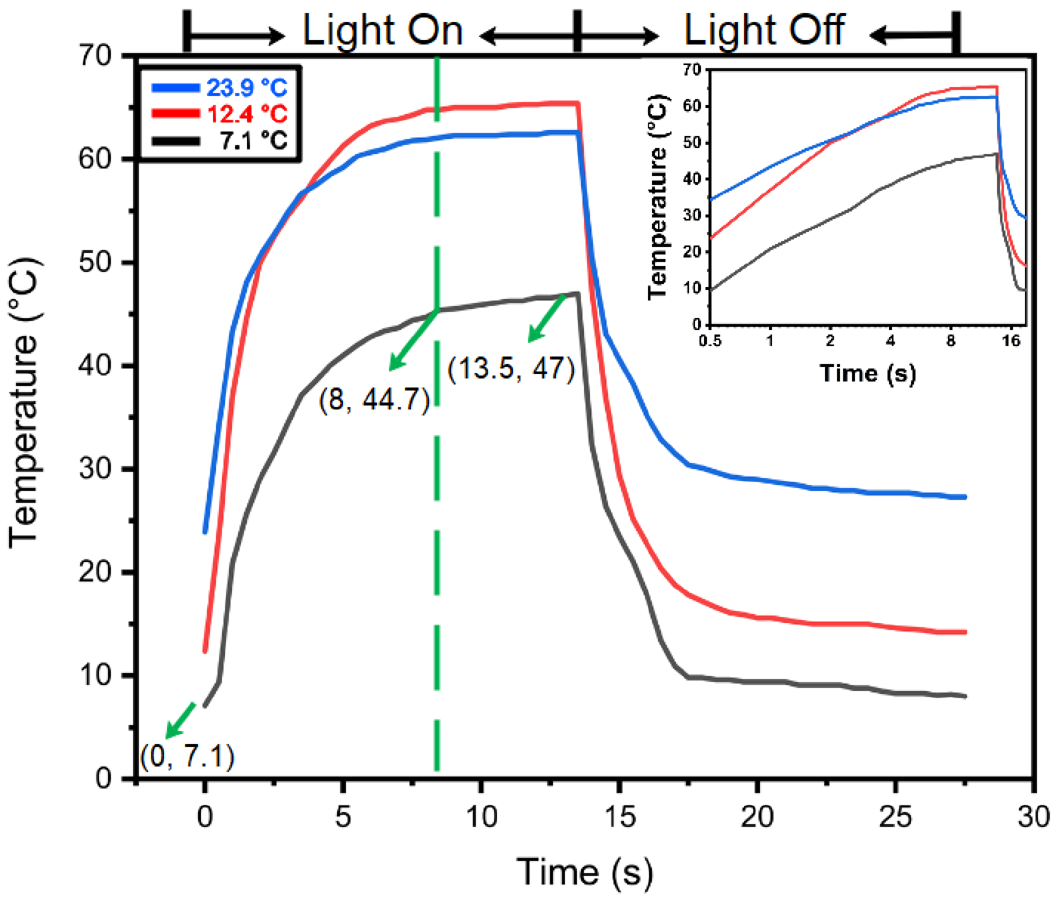

Fig. 3. Photothermal performance of the photothermal composite at different environment temperatures. Line graph showing the surface temperature of the sponge doped with graphene versus time at different ambient temperatures, with normal time axis and logarithm time axis (the inset graph). The *T*–*t* curve shows an approximate exponential decay in both exposure and non-exposure periods.

Table 1. Movement performances in various irradiation programs.

IRRADIATION/ RELAXATION RATIO*	AVERAGED HORIZONTAL VELOCITY (mm s^{-1})	ENERGY EFFICIENCY (10^{-7})
3 s/5 s	7.6	2.0
4 s/5 s	6.6	1.1
4 s/6 s	7.9	1.6
4 s/7 s	6.5	1.1
5 s/6 s	6.4	0.9
5 s/7 s	7.7	1.2
5 s/8 s	8.0	1.3
6 s/5 s	13.1	3.0
6 s/6 s	12.2	2.6
7 s/6 s	11.0	1.8
8 s/5 s	9.2	1.1
8 s/6 s	11.7	1.8
9 s/6 s	10.9	1.4

Footnotes: The active/passive transport time ratio* is a feature of a periodic irradiation program. For example, the 6 s/5 s ratio represents a periodic irradiation program of 6 s light on, 5 s light off, 6 s light on, 5 s light off and so on periodically.

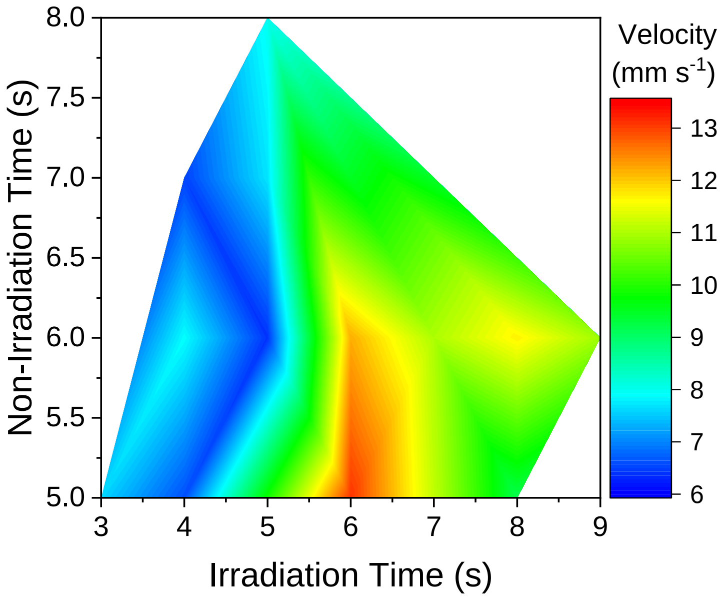

Fig. X. Mapping PPFR velocity versus irradiation/non-irradiation program.

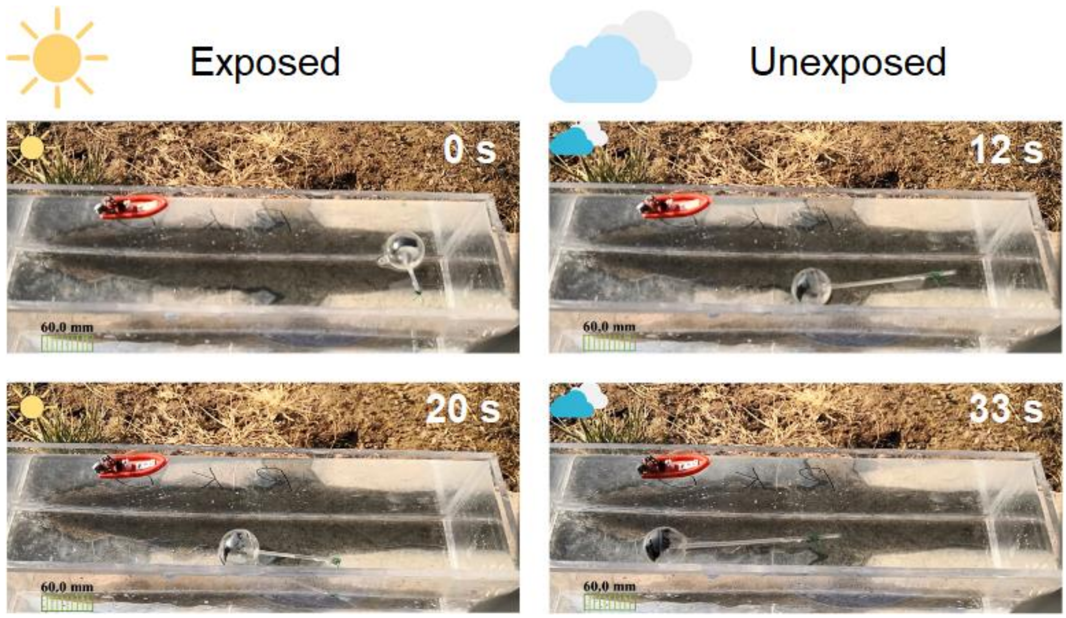

Fig. 4. Sunlight driving PPFR. Digital images showing a PPFR swimming, when it is exposed and unexposed to outdoor sunlight alternately. The average swimming speed achieves 9.6 mm s^{-1}.

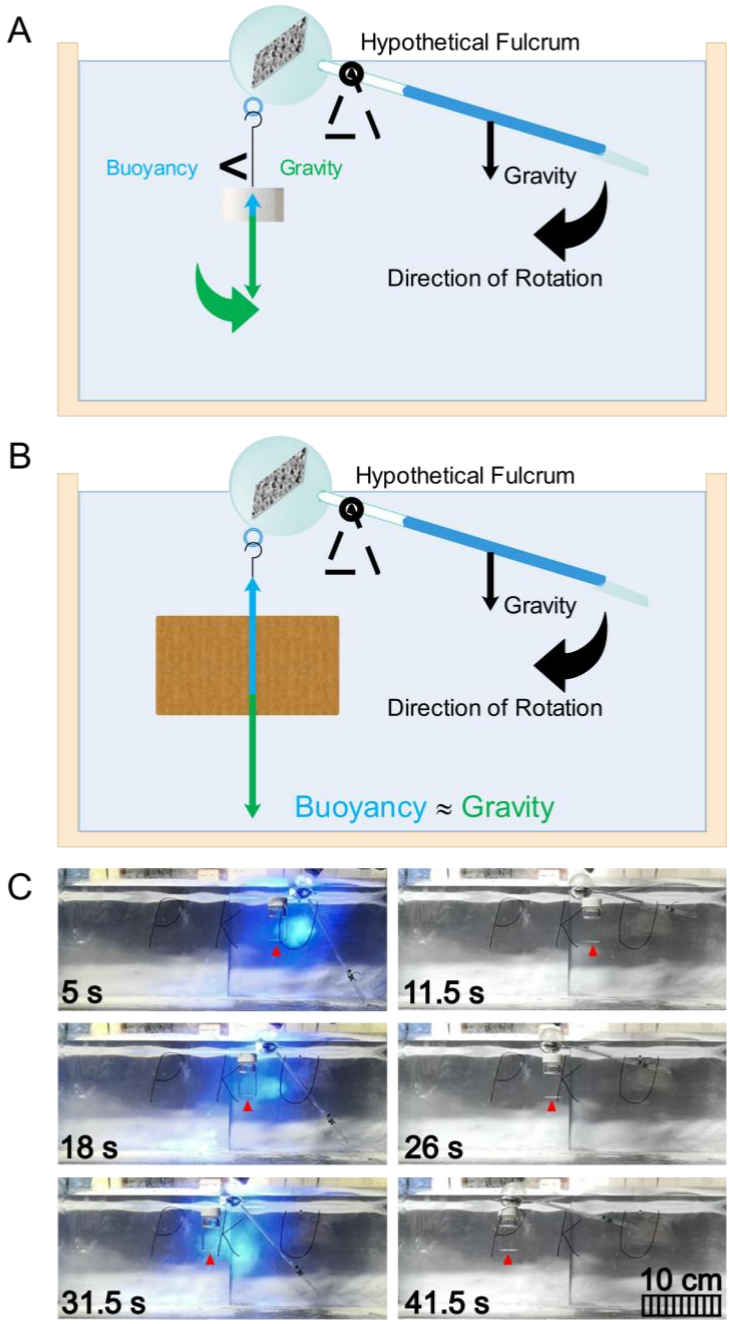

Fig. 5. Leverage model and images of the loading experiment of PPFR. (**A** and **B**) Leverage models to explain how the density of load influences the rotation of the PPFR paddle. (**C**) Digital images showing one 8.3 g PPFR runs at an average speed of 3.9 mm s^{-1} with a 31.7 g load. The load density is about equal water density. The irradiation is a 365 nm light with a power density of 170 mW cm^{-2}.

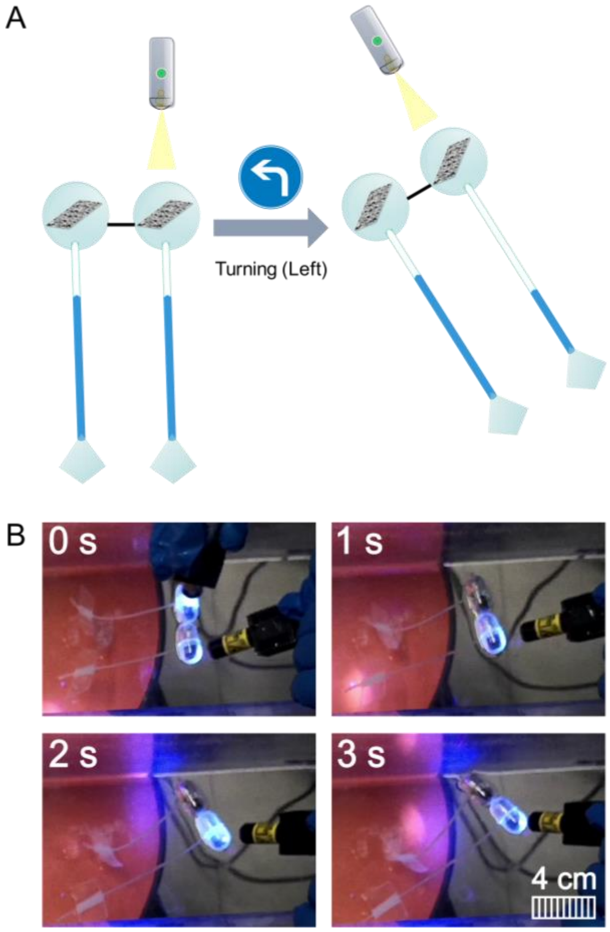

Fig. 6. The integration and on-demand control of PPFRs. (**A**) Schematic illustration of the on-demand turning PPFR pair developed with differential steering. (**B**) Digital images showing a PPFR pair turning left controlled with light.

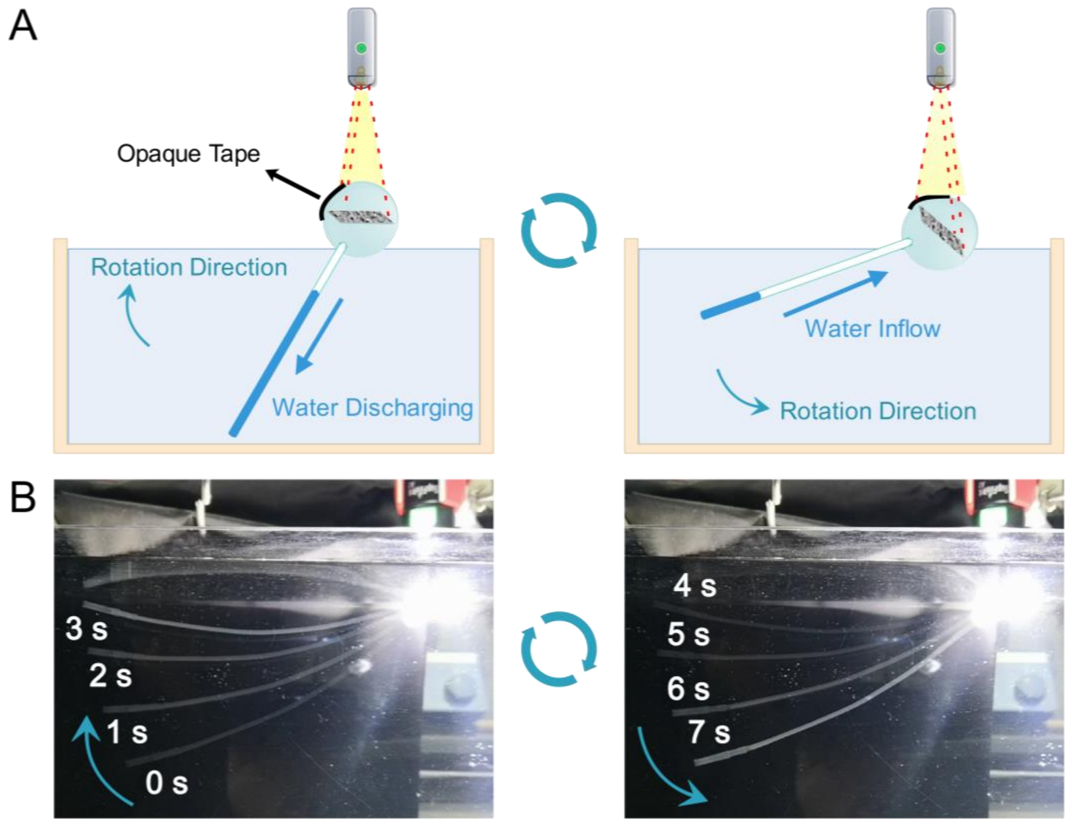

Fig. 7. Self-sustained oscillating PPFR. (**A**) Schematic illustration of the self-sustained light-driven movement of a self-shadowing-enabled PPFR. (**B**) Continuous superposed digital images of a self-sustained oscillating light-driven PPFR without a paddle.

SUPPLEMENTARY MATERIALS

Fig. S1. UV-vis absorption spectra and images of graphene doped sponge and pure sponge.

Movie S1. PPFR swimming at its resonance ratio in an indoor experiment.

Movie S2. High-speed sunlight-driven PPFR swimming in an outdoor experiment.

Movie S3. Heavy-load PPFR swimming.

Movie S4. A PPFR pair turning left with differential steering.

Movie S5. Self-sustained oscillating PPFR.